PROTEINS
STRUCTURE ■ FUNCTION ■ BIOINFORMATICS

A2T and A2V Aβ peptides exhibit different aggregation kinetics, primary nucleation, morphology, structure, and LTP inhibition

Brian Murray,[1] Mirco Sorci,[1] Joseph Rosenthal,[2] Jennifer Lippens,[3] David Isaacson,[2] Payel Das,[4] Daniele Fabris,[3] Shaomin Li,[5] and Georges Belfort[1]*

[1] Department of Chemical and Biological Engineering and Center for Biotechnology and Interdisciplinary Studies, Rensselaer Polytechnic Institute, Troy, New York 12180

[2] Department of Mathematical Sciences, Rensselaer Polytechnic Institute, Troy, New York 12180

[3] Department of Chemistry, University at Albany, State University of New York, Albany, New York 12222

[4] Soft Matter Theory and Simulations Group, Computational Biology Center, IBM Thomas J. Watson Research Center, Yorktown Heights, New York 10598

[5] Center for Neurologic Diseases, Brigham and Women's Hospital and Harvard Medical School, Boston, Massachusetts 02115

ABSTRACT

The histopathological hallmark of Alzheimer's disease (AD) is the aggregation and accumulation of the amyloid beta peptide (Aβ) into misfolded oligomers and fibrils. Here we examine the biophysical properties of a protective Aβ variant against AD, A2T, and a causative mutation, A2V, along with the wild type (WT) peptide. The main finding here is that the A2V native monomer is more stable than both A2T and WT, and this manifests itself in different biophysical behaviors: the kinetics of aggregation, the initial monomer conversion to an aggregation prone state (primary nucleation), the abundances of oligomers, and extended conformations. Aggregation reaction modeling of the conversion kinetics from native monomers to fibrils predicts the enhanced stability of the A2V monomer, while ion mobility spectrometry-mass spectrometry measures this directly confirming earlier predictions. Additionally, unique morphologies of the A2T aggregates are observed using atomic force microscopy, providing a basis for the reduction in long term potentiation inhibition of hippocampal cells for A2T compared with A2V and the wild type (WT) peptide. The stability difference of the A2V monomer and the difference in aggregate morphology for A2T (both compared with WT) are offered as alternate explanations for their pathological effects.

Proteins 2016; 84:488–500.

Key words: Alzheimer's disease (AD); amyloid; protective mutation; abeta A2T and A2V; abeta oligomers.

INTRODUCTION

The molecular process underlying AD, according to the abeta peptide hypothesis, involves an imbalance between production and clearance of amyloid beta peptide (Aβ). Different lengths of Aβ are generated by proteolytic cleavage of the amyloid precursor protein (APP), and subsequently removed from the brain by one of several paths including binding to apolipoprotein E (ApoE) via receptor-mediated endocytosis. The abnormal aggregation of the Aβ peptides into β-sheet rich small and large aggregates, protofibrils and fibrils involves a heterogeneous ensemble of oligomeric intermediates, all of which are found to be neurotoxic.[1,2]

A critical barrier to progress is the lack of accepted mechanism-based treatments for AD.[3,4] In our search for molecular mechanisms involving Aβ production, aggregation, toxicity, and clearance, we are motivated by several recent seminal findings: (i) the existence of a protective APP variant [A673T in APP or A2T in $A\beta_{1-42}$];[5,6] (ii) an earlier reported less polar A673V APP/A2V $A\beta_{1-42}$ mutation at the same site causes dementia and affects its biophysical properties;[7,8] (iii) the purported reversal of amyloidosis in mice

Additional Supporting Information may be found in the online version of this article.

Grant sponsor: NIH; Grant number: GM0,64328–14; Grant sponsor: RPI's Institute Chair Funds.

This article was published online on 23 February 2016. An error was subsequently identified. This notice is included in the online and print versions to indicate that both have been corrected 30 April 2016.

*Correspondence to: Georges Belfort, Department of Chemical and Biological Engineering and Center for Biotechnology and Interdisciplinary Studies, Rensselaer Polytechnic Institute, Troy, NY 12180. E-mail: belfog@rpi.edu

Received 6 October 2015; Revised 23 December 2015; Accepted 11 January 2016
Published online 21 January 2016 in Wiley Online Library (wileyonlinelibrary.com). DOI: 10.1002/prot.24995

transgenic models of AD through clearance of Aβ via up-regulation of the ApoE gene;[9] and (iv) the recent findings of receptor-mediated synaptotoxic pathways prompted by $A\beta_{1-42}$ binding lead to synaptic impairment.[10–13] As a consequence of these findings, devoting attention to molecular events downstream of the cleavage of APP and the subsequent biophysical properties of Aβ seems appropriate. Clearly, reducing the upstream production of Aβ and facilitating effective clearance are reasonable goals for reducing AD.[14,15] Two recent reports have shown that the A2T variant affects β-secretase cleavage producing 20% lower amounts of both $A\beta_{1-42}$ and $A\beta_{1-40}$ and that aggregation rates differ for A2T and A2V variants of $A\beta_{1-42}$.[16,17] Their kinetic results do not agree between them nor do they agree with the results presented here (see below).

In the human brain,[18] the protective variant (A2T) is expressed together with a wild-type (WT) copy of the gene resulting in only a ∼20% decrease in total $A\beta_{1-42}$ concentration (A2T + WT).[5] Hence, the prevailing hypothesis for its protective action is that the mutation (A2T) is close to the cleavage site of the enzyme complex β-secretase, and thus lowers $A\beta_{1-42}$ production. To our knowledge, there is no direct evidence connecting a drop of ∼20% with a mechanism of protection.[18] Also, earlier results indicate that the A2V mutation affects Aβ aggregation kinetics and causes dementia only in people in which both gene copies are mutated, not just one.[7,18]

The purported reversal of AD in a mouse model with the addition of a retinoid X receptor agonist, bexarotene, that overproduced ApoE protein and effectively scavenged Aβ from the brain, demonstrated that effective downstream clearance can be critical for the reversal of AD in a mouse.[9] Note that reproducing this finding *in toto* has been difficult.[19] Only one group that used the exact same formulation of bexarotene was able to "confirm the reversal of memory deficits in APP/PS1DE9 mice expressing human ApoE3 or ApoE4 to the levels of their non-transgenic controls and the significant decrease of interstitial fluid Aβ, but not the effects on amyloid deposition."[20]

Several recent reports demonstrate that $A\beta_{1-42}$ (mainly in its oligomeric form) binds to PrPc, EphB2, FcγRIIB, LilrB2, and NMDAR.[10,11] Reversing EphB2 depletion, caused by Aβ oligomers, recovers memory loss in mouse models of AD.[21] Apparently, NMDAR is affected indirectly through PrPc and EphB2, while FcγRIIB and LilrB2 are directly involved sending a signal into the cell with subsequent cell death.[10]

Our aim is to connect these four recent findings in a cogent and consistent account with relevance to AD by characterizing the *in vitro* biophysical behavior of the $A\beta_{1-42}$ variants at the molecular level during aggregation in solution, and interacting with ApoE isoforms and a receptor domain in solution. To do this, we develop an aggregation reaction model to help quantify the downstream aggregation, mimic clearance and synaptotoxic events, and measure the formation of spherical and protofibril aggregates. We also utilize ion mobility spectrometry mass spectrometry (IMS-MS) to compare the structural behavior of these variant monomers. The results presented here are direct *in vitro* evidence supporting the hypothesis that protective and causative variants of $A\beta_{1-42}$ aggregate with structural differences induce toxicity to neuronal cells differently, bind to ApoE isoforms and to receptor domains differently. The results clearly implicate molecular structural differences (and subsequent differences in aggregate shape) in obtaining protection or causation of cell toxicity resulting from a single mutation in the N-terminal region of $A\beta_{1-42}$.

MATERIALS AND METHODS

Materials

Aggregation

$A\beta_{1-42}$ (Cat #: 62–0–80B) and $A\beta_{1-42}$ scrambled sequence (Cat #: 62–0–46B) were purchased from American Peptide (Sunnyvale, CA) and were received as lyophilized powder verified to >97% purity with HPLC by American Peptide. $A\beta_{1-42}$ variant peptides, A2T and A2V, were purchased as custom orders from American peptide, and were received as lyophilized powders verified >90% purity by using HPLC by American Peptide. Thioflavin T (Cat #: 2390–54–7) was purchased from Sigma Aldrich (St Louis, MO). Phosphate buffer saline tablets (PBS) (Cat #: P4417) were purchased from Sigma Aldrich. Synergy HT microplate readder (Biotek Instruments™, Winooski, VT) was used to read twin.tec 96 skirted LoBind plates (Cat #: 0,030129 512) purchased from Eppendorf North America (Hauppauge, NY). IMS-MS analysis was performed using a Synapt G2 HDMS (Waters, Milford, MA). Ammonium acetate (Cat #: 631–61–8) was purchased from Sigma Aldrich. Coomassie (Bradford) Protein Assay Kit (Cat#: 23200) was purchased from Thermo Scientific.

Dot blots

ApoE3 and E4, produced recombinantly, were generous gifts from Dr. Jianjun Wang, Wayne State University, School of Medicine (Detroit, MI). EphB2-FC chimera (Cat #: 467-B2–200) were purchased from R&D Systems (Minneapolis, MN). The sequence-specific primary antibody used for the detection of $A\beta_{1-42}$ is the Beta-Amyloid, 17–24 (4G8) Monoclonal Antibody (Cat #: SIG-39220) from Covance (Dedham, MA). The secondary antibody, AP Conjugate, Anti-(Mouse IgG + IgM), Raised in Goat (Cat #: T2192) and the secondary antibody detection kit [Pierce ECL Western Blotting Substrate (Cat #: 32106, Thermo Scientific, Rockford, IL)] were purchased from Life Technologies (Grand Island, NY). Nonfat milk powder used for dot-blot blocking was purchased from a grocery store. Amersham™

Hybond^{TM}-ECL membranes (Cat #: RPN2020D) were purchased from GE Healthcare Lifesciences (Pittsburgh, PA).

Hippocampal slice preparations

Mice were sacrificed by isoflurane anesthesia at age 6–8 weeks. Brains were quickly removed and submerged in ice-cold oxygenated sucrose-replaced artificial cerebrospinal fluid (ACSF) cutting solution containing (in mM) 206 sucrose, 2 KCl, 2 $MgSO_4$, 1.25 NaH_2PO_4, 1 $CaCl_2$, 1 $MgCl_2$, 26 $NaHCO_3$, 10 d-glucose, pH 7.4, 315 mOsm). Transverse slices (350-μm thick) were cut with a vibroslicer from the middle portion of each hippocampus. After dissection, slices were incubated in ACSF containing (in mM): 124 NaCl, 2 KCl, 2 $MgSO_4$, 1.25 NaH_2PO_4, 2.5 $CaCl_2$, 26 $NaHCO_3$, 10 D-glucose, pH 7.4, 310 mOsm, in which they were allowed to recover for at least 90 min before recording. A single slice was then transferred to the recording chamber and submerged beneath continuously perfused ACSF saturated with 95% O_2 and 5% CO_2. Slices were incubated in this chamber for 20 min before stimulation at RT (~24°C).

Methods

Aggregation

$A\beta_{1–42}$ was aliquoted into 50 μg aliquots by dissolving the total peptide to a concentration of 1 mg mL^{-1} with 50/50 volume ratio acetonitrile/water. The aliquots were lyophilized overnight to remove the acetonitrile/water solvent. To prepare the $A\beta_{1–42}$ for use, the aliquots were removed from the freezer and dissolved to 1 mg mL^{-1} in hexafluoroisopropanol (HFIP). The HFIP was evaporated under a low pressure stream of N_2 for at least 10 min generating a peptide film. Next, the peptide was redissolved in 50 μL of 50 mM NaOH and then sonicated in an ice-bath for 15 min. Nearly 400 μL of pre-pH adjusted PBS was added to solution so that the final pH was 7.4. An additional 15 min ice-bath sonication was conducted followed by ultracentrifugation at 4°C, 70,000 rpm, for 30 min using an ultracentrifuge (OPTIMA MAX-XP, Beckman Coulter, Brea, CA) with a TLA 100.3 rotor. 350 μL of supernatant was removed for further use. Aggregation was performed with 100 μL of 12.5 μM $A\beta_{1–42}$ with 10 μM ThT *in situ* per well in a twin.tec 96 skirted LoBind plate. Peptide concentration was confirmed using Bradford assay. Aggregation experiments were performed at 37°C using either mixing (1020 rpm) or no mixing with four replicates. ThT fluorescence, used to track amyloid aggregation,[22] was measured at 440/485 nm excitation/emission with a gain of 50 and read height of 1 mm.

Atomic force microscopy (AFM)

Images of $A\beta_{1–42}$ were collected with an MFP-3D atomic force microscope (Asylum Research, Santa Barbara, CA) and standard Si cantilevers (AC240TS, Olympus America, Center Valley, PA). Samples were prepared by depositing 10 μL of $A\beta_{1–42}$ collected from the end of the aggregation runs in Figure 1 onto mica slides. The slides were washed for 3 min with DI H_2O and allowed to air dry before imaging. Three-dimensional measurements were collected in air using the tapping mode technique of AFM and analyzed with IGOR Pro 5 (WaveMetrics, Lake Oswego, OR).

Hippocampal slice electrophysiology

Standard field EPSPs (fEPSPs) were measured from the CA1 region of the hippocampus using a previously described protocol.[23–25] A bipolar stimulating electrode (FHC, Bowdoin, ME) was placed in the Schaffer collaterals to deliver test and conditioning stimuli. A borosilicate glass recording electrode filled with ACSF was positioned in stratum radiatum of CA1, 200–300 μm from the stimulating electrode. fEPSP in CA1 were induced by test stimuli at 0.05 Hz with an intensity that elicited a fEPSP amplitude of 40–50% of maximum. Test responses were recorded for 30–60 min prior to beginning the experiment, to ensure stability of the response. To induce LTP, two consecutive trains (1 s) of stimuli at 100 Hz separated by 20 s, a protocol that induces LTP lasting ~1.5 h in wild-type mice of this genetic background were applied to the slices. All LTP values represent fEPSP slopes measured 60 min after the conditioning stimulus ($n = 6$). The field potentials were amplified 100× using Axon Instruments 200B amplifer and digitized with Digidata 1322A. The data were sampled at 10 kHz and filtered at 2 kHz. Traces were obtained by pClamp 9.2 and analyzed using the Clampfit 9.2. Two-tailed Student's *t*-test and one-way analysis of variance (ANOVA) were used to determine statistical significance.

Stock solutions of 500 μM $A\beta_{1–42}$ were prepared 3 h before LTP recordings. Prior to LTP recording, 10 μL of $A\beta_{1–42}$ stock was added to 10 mL of perfusion ACSF, bringing the final $A\beta_{1–42}$ concentration to 500 nM. Brain slices for the control LTP were tested daily whenever compounds were added to the buffer to make sure the brain slices were healthy and exhibited normal LTP. Our control LTP level was around 150% (see Fig. 3 and Refs. 23,25). We (co-author, Li from the Selkoe Lab) have previously demonstrated that for immunodepleted cells, the soluble WT Aβ oligomers can restore the LTP,[26] therefore, it was suggested that Aβ is the key synaptotoxic agent for LTP inhibition. When the A2T and A2V mutants were added into the perfusion buffer, the LTP baseline did not change and was stable up for up to 2 h (data not shown).

Circular dichroism (CD)

Spectra were collected using a Jasco 815 CD Spectrometer (Jasco, Easton, MD) with a Spectrosil® Far UV Quartz cuvette (Starna Cells, Atascaddero, CA, Cat #: 21-Q-1).

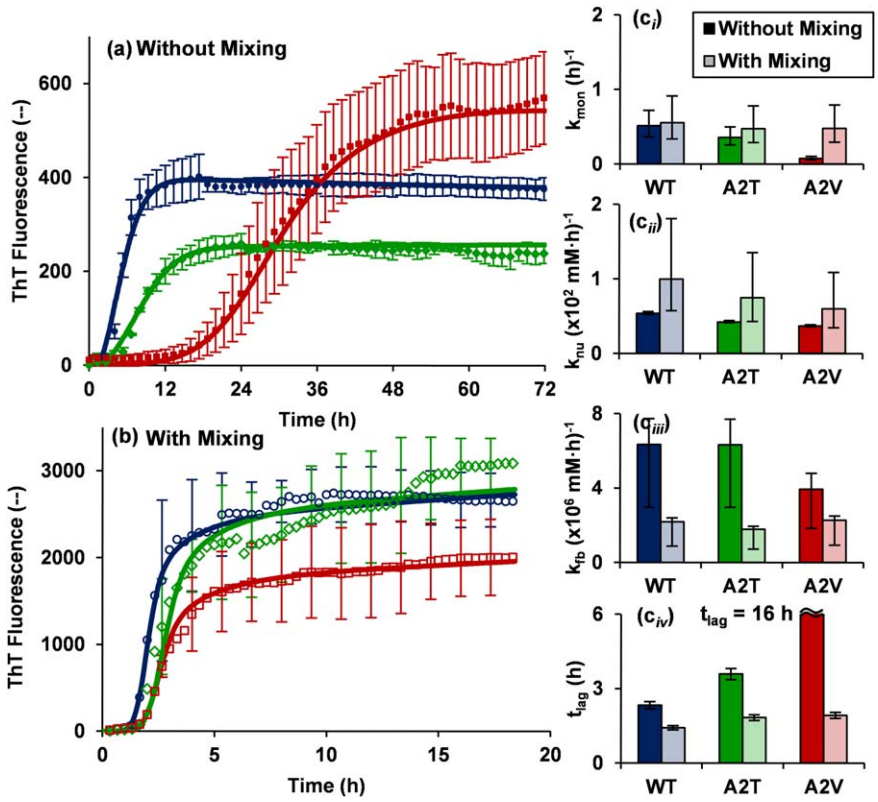

Figure 1

Aggregation kinetics and modeling: WT (blue circles), A2T (green diamonds) and A2V (red squares) aggregation kinetics (**a**) without mixing (solid symbols) and (**b**) with mixing (open symbols). The model fit of the data for fibrils are the solid lines. The fit of the model to the data are described by $R^2 = 0.9888$, $R^2 = 0.9912$, and $R^2 = 0.9961$ for WT, A2T, and A2V, respectively, for non-mixing and by $R^2 = 0.9923$, $R^2 = 0.9547$, and $R^2 = 0.9950$ for WT, A2T, and A2V, respectively, for mixing. Experimental data are the average values of $n = 4$ aggregation runs, and the error bars represent ± 1 standard deviation. (*ci–civ*) Rate constants from the aggregation reaction model. The rate constant error is derived from fitting of individual runs of the WT data, and scaled to A2T and A2V. The remaining reaction model parameters are given in Supporting Information Tables SI and SII. [Color figure can be viewed in the online issue, which is available at wileyonlinelibrary.com.]

Samples were prepared using the same protocol from the aggregation experiments except substituting 10 mM PB buffer for PBS buffer to greatly reduce the salt concentration. Measurements were taken at 21°C using ten accumulations. Spectra were read from 240 to 195 nm with a 1.0 nm band width, a sensitivity of 100 mdeg, a response of 1 s, and a scan speed of 100 nm min^{-1}.

Ion mobility spectrometry-mass spectrometry

All samples were analyzed by direct infusion nanoflow ESI on a Waters (Milford, MA) Synapt G2 HDMS instrument capable of providing both molecular mass and ion mobility data. Nanospray operations involved the utilization of quartz emitters produced in house by a Sutter Instruments Co. (Novato, CA) P2000 laser pipette puller. Up to 5 μL samples were typically loaded onto each emitter by using a gel-loading pipette tip. A stainless steel wire was inserted in the back-end of the emitter to supply an ionizing voltage that ranged between 0.4 and 0.8 kV. Experimental/instrumental conditions were kept consistent in all experiments and consisted of a cone voltage of 60 V, a source temperature of 30°C, a wave velocity of 650 m s^{-1}, and a wave height of 40 V. For all samples, both mass and arrival time data were collected respectively in the mass over charge (m z^{-1}) scale and time dimension. Samples of the three variants (WT, A2T, and A2V) were analyzed in 150 mM ammonium acetate solution (pH adjusted to 7.0) at final peptide concentrations of 5 μM. Each variant was left to equilibrate in solution for >15 min on ice prior to eventual IMS-MS analysis. Based on the observation that the three $A\beta_{1-42}$ peptides share a pI of about 5.0,[27] the samples were analyzed in negative ion mode.

Dot blots

A 2 μL of 25 μM protein, either $A\beta_{1-42}$, ApoE3 or E4, or EphB2-FC chimera was blotted on a Hybond™-ECL membrane. Blots were allowed to air dry at RT. Membranes were then blocked with 10% nonfat milk in PBS buffer for 2 h at RT. The membranes were washed four times for 5 min with PBS buffer, which was used as the standard wash step. A 2.5 μM of Aβ WT monomer or variant in PBS at pH 7.4 was incubated overnight (at least

Table I
Reaction diagram and species reactions for the primary nucleation aggregation reaction model

Reaction Diagram

$$A_0 \underset{k_{mon-}}{\overset{k_{mon}}{\rightleftharpoons}} A_1 \quad (1)$$

$$A_i + A_1 \rightarrow A_2 \text{ (}k_{on2}\text{, } k_{on2-}\text{, } k^*_{off}\text{)}, \quad A_i + A_1 \rightarrow \text{off-path} \quad (2)$$

$$A_i + A_1 \underset{k_{nu-}}{\overset{k_{nu}}{\rightleftharpoons}} A_{i+1} \quad (3)$$

$$F + A_i \underset{k_{fb-}}{\overset{k_{fb}}{\rightleftharpoons}} F \quad (4)$$

$$F \xrightarrow{k_{frag}} F + F \quad (5)$$

Species Reactions

$$\frac{dA_0}{dt} = -J_{mon}, \quad (6)$$

$$\frac{dA_1}{dt} = -J_{mon} - \sum_{i=1}^{5} J_{nu,i} - J_{nu,1} - J_{fb,1} - 2J^*_{off}, \quad (7)$$

$$\frac{dA_i}{dt} = -J_{nu,i} + J_{nu,i-1} - J_{fb,i}, \quad i = 2, 3, 4, 5 \quad (8)$$

$$\frac{dF}{dt} = J_{nu,5} + J_{frag}, \quad (9)$$

Species Fluxes

$$J_{mon} = k_{mon}A_0 - k_{mon-}A_1, \quad (10)$$

$$J_{nu,i} = k_{nu}A_1A_i - k_{nu-}A_{i+1}, \quad (11)$$

$$J_{fb,i} = k_{fb}FA_i - k_{fb-}F, \quad (12)$$

$$J_{frag} = k_{frag}F, \quad (13)$$

$$J^*_{off} = k^*_{off}A_1^2 \quad (14)$$

12 h) at RT. The membranes were washed with PBS followed by an incubation with 1:5000 primary antibody for 1 h at RT. Another wash step was performed and the membranes were subsequently incubated with 1:10000 secondary antibody for 1 h at RT. Membranes were washed again, followed by development and film exposure for ~ 10 s. Blot results were quantified using the "Dot Blot Analyzer" macro for ImageJ, NIH. A rolling background subtraction of 40 with a dot radius of 5 was used for analysis.

Aggregation reaction model

Primary nucleation is defined as the process in which monomers nucleate in solution forming precursors for fibrillation. Cohen *et al.* suggest that monomer-dependent secondary nucleation is the dominant mechanism for $A\beta_{1-42}$ aggregation during which Aβ fibrils catalyze the formation of new ones.[28] Ferrone posits that this process must involve a monomeric conformational change, the conformational change is the aggregation's overall rate limiting step, that the nuclei must be monomeric and that the assembly process after the rate-limiting conformational change is "downhill despite clear lag times and significant concentration dependence."[29] Others have reported that the two $A\beta_{1-42}$ variants (A2T and A2V) and wild type (WT) exhibited negligible differences in aggregation rates with little or non-measurable quiescent lag times, indicating the secondary nucleation rates were identical for all three variants.[16,17] Here we have performed aggregation experiments using a protocol designed to prevent seeded aggregation, that is, forcing primary nucleation to occur first, and have modeled these aggregation processes using a set of equations that specifically describes amyloid primary nucleation kinetics, predicts the concentration profiles of all small oligomeric species during aggregation and includes an "off-path" reaction (Table I).

The primary nucleation reaction model with fibril fragmentation is fit to the experimental aggregation data in Figure 1. It is adapted from a previously published model for the amyloid insulin's conversion reactions[30] and is based on the following assumptions: (i) an initial, reversible conformational change of the $A\beta_{1-42}$ monomer, (ii) unfolded monomers add to each other and species of size i to form species of size $i+1$, (iii) conversion reactions from monomer to fibril under mixing conditions is assumed to be complete and follows an on-pathway reaction, that is, all the monomer is sequestered into fibril, not other aggregate species, at the end of the run [Fig. 2(A)]. For non-mixing, only a fraction of the initial monomer follows the on-pathway, as estimated from the final asymptotic thioflavin T (ThT) values at long times, the rest of the monomer, dimer, trimer, and so forth detour to an off-pathway reaction under the control of k^*_{off} forming small (WT) and large (A2V) spherical-like aggregates or protofibrils (A2T) [Fig. 2(B,C)]. (iv) Fibrils fragment to shorter fibrils.[28] (v) All fibrils are accounted for as F due to publications by Serio *et al.* and Heldt *et al.* demonstrating fibrils of all length undergo reactions mostly at the two fibril ends.[31,32] A complete picture of the reaction diagram and species reactions are given in Table I.

Using MatLab (The MathWorks, Natick, MA), nonlinear least-squares regression was utilized to minimize the sum of squared errors between the experimental data and those predicted by the model through estimation of k_{mon}, k_{mon-}, (forward and reverse monomer unfolding rate constants) k_{nu}, k_{nu-}, (forward and reverse primary nucleation rate constants) k_{fb}, k_{fb-}, (forward and reverse fibrillation rate constants) k_{frag}, (fragmentation rate constant) and k^*_{off} (off path rate constant). To determine the reverse rate constants, k_{frag} and k^*_{off}, all parameters were fit to four different concentrations of WT kinetics for the cases of aggregation with mixing and without mixing while k_{mon-}, k_{nu-}, k_{fb-}, k_{frag}, and k^*_{off} were assumed to remain constant for all aggregation runs of each case (Supporting Information Fig. S1). Once those five rate constants were determined, the three remaining forward rate constants (k_{mon}, k_{nu}, and k_{fb}) were estimated by fitting the model to the data in Figure 1(A,B). The complete set of rate constants for each experimental condition is presented in Supporting Information Tables SI and SII.

RESULTS

In this work, we compared the *in vitro* biophysical behavior of the protective and causative $A\beta_{1-42}$ variants (A2T and

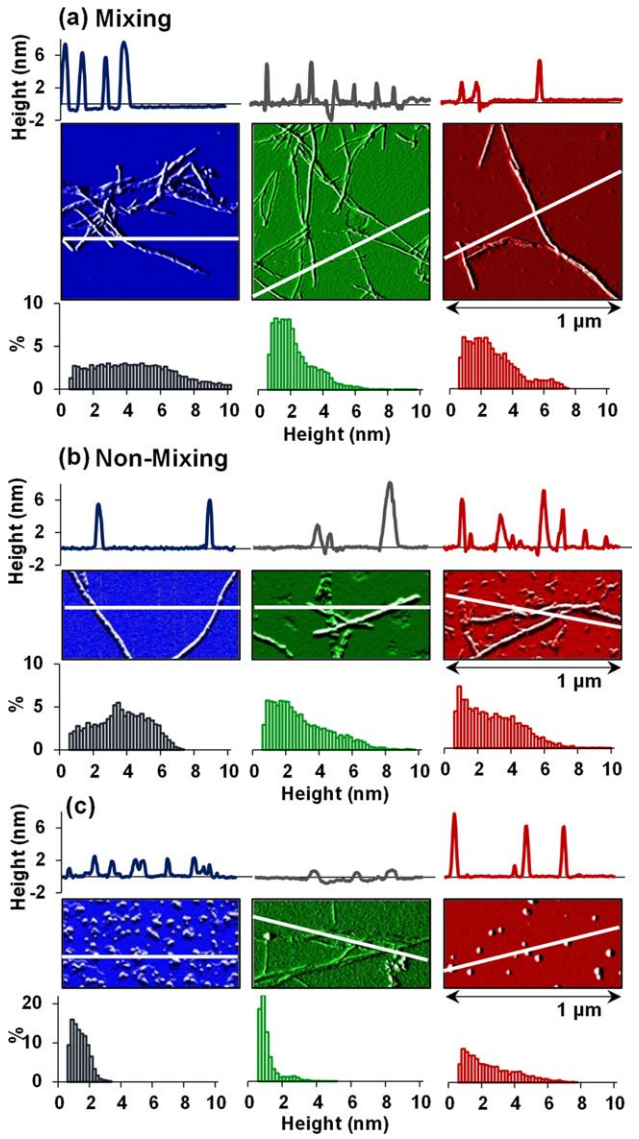

Figure 2

Aggregate Morphology and Height: AFM images of $A\beta_{1-42}$ aggregates formed with (**a**) mixing: fibrils, (**b**) non-mixing: fibrils, and (**c**) non-mixing: other aggregates. About 10 μL samples of 12 μM $A\beta_{1-42}$ WT (left column), A2T (middle column), and A2V (right column) collected at the end of the aggregation runs from Figure 1 were deposited onto mica and the images were collected in air. Line height analysis (above) displays the height of each pixel in contact with the solid white line on each image moving from left to right. Histogram height analysis (below) represents the height distribution of all aggregates above 500 pm in each image. [Color figure can be viewed in the online issue, which is available at wileyonlinelibrary.com.]

A2V) with that of wild type (WT) in order to determine differences in molecular properties by measuring the aggregation kinetics (ThT), oligomer morphology (Atomic Force Microscopy, AFM), LTP inhibition (standard field excitatory postsynaptic potential, fEPSP), and monomeric structure (circular dichroism, CD and ion mobility spectrometry-mass spectrometry, IMS-MS). Also, by fitting an aggregation reaction model to the aggregation kinetics data, different oligomer species (dimers, trimers, and so forth) were tracked and the reaction rate constants for the different variants estimated. We further estimated binding to ApoE (with relevance to *in vivo* modulation of $A\beta_{1-42}$ levels)[33] and to the receptor EphB2 domain (with implications for neuron receptor function)[21] of the variants, with a focus on understanding the protection and causation effects.

Aggregation kinetics and morphology of oligomers

The mechanism of fibril formation changes from one where breakage occurs and fibrils multiply (mixing) to one where secondary nucleation dominates (quiescent—non-mixing).[34] A comparison of the kinetic aggregation data, the aggregation reaction model fits to the data with kinetic rate constants (Fig. 1) and AFM images with analysis of the aggregate morphology at the end-point of

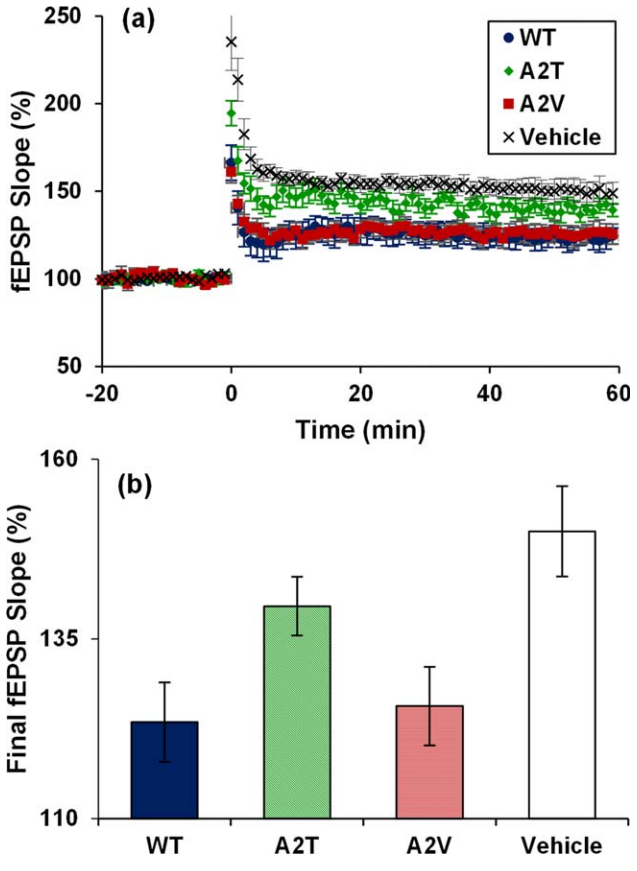

Figure 3

LTP inhibition: (**a**) Aβ1–42 WT (blue circles), A2T (green diamonds), A2V (red squares), and vehicle (ACSF, black 'x's) inhibition of LTP of neurons from the CA1 hippocampal region induced by high frequency stimulation (HFS, t = 0 min). Error bars represent ± 1 SEM (n = 6) (**b**) Final fEPSP slope calculated from the average of the final five readings from (A), with the error bar representing the average standard deviation of the final six data points.[Color figure can be viewed in the online issue, which is available at wileyonlinelibrary.com.]

the runs for WT, A2T and A2V with and without mixing (Fig. 2) is presented. These asymptotic ThT values exhibit a linear increase with respect to $A\beta_{1-42}$ concentration (Supporting Information Fig. S2).

Comparison of aggregation kinetics

Aggregation of $A\beta_{1-42}$ variants at 37°C without mixing reveals WT aggregates with a lag time to fibril onset, t_{lag}, of 2.3 ± 0.13 h, while A2T aggregates slower (3.6 ± 0.19 h) and A2V decidedly slower still [16 ± 1.0 h, Fig. 1(A)]. The reaction model predicts the decrease in overall aggregation rate is primarily due to a 31% decrease in k_{mon} for A2T and an 86% decrease in k_{mon} for A2V compared with WT. For reference, there is at most a 33% reduction in k_{nu} and an 38% reduction in k_{fb} for A2V compared with WT. Also, fragmentation could have occurred but was not incorporated into the model (i.e., we did not separately measure nor relate fragmentation to average shear rate during mixing).

Decreases in k_{mon} coincide with the idea of a more stable initial monomer for A2V. Increased stability of the A2V monomer is consistent with results from a recent molecular dynamics study where it was shown that A2V is decidedly more stable due to the monomer sampling an increased number of conformations with long range hydrophobic interactions compared with WT and A2T.[35]

Comparing mixing [1020 rpm, 37°C, Fig. 1(B)] with non-mixing [0 rpm, 37°C, Fig. 1(A)] for the $A\beta_{1-42}$ variants in solution gave the following results: (i) As expected, mixing significantly speeded up t_{lag} as compared with nonmixing.[36] (ii) Tracking the kinetics via β-sheet formation (ThT), the trajectories with error bars ($n = 4$) for mixing are close to each other whereas the aggregation kinetics are clearly distinct for non-mixing. It should be noted the large error bars are due to the heterogeneous nature of Aβ aggregation. (iii) The final ThT asymptotes are five to eight times higher for the mixing versus nonmixing.[37] Because all the initial monomer (12.5 μM $A\beta_{1-42}$) for each variant is assumed to convert to fibrils during mixing [Fig. 2(A), we consider this a complete on-pathway reaction, $k^*_{off} = 0$, in the aggregation reaction model], we estimate from the long-time asymptotic values between mixing [Fig. 1(B)] and nonmixing [Fig. 1(A)] that, for non-mixing, only about 14.6% of the WT oligomers are on-path with $k^*_{off} = 0$. The rest is off-path ($k^*_{off} > 0$). (iv) k_{mon} is the slowest rate constant by orders of magnitude making it the overall rate limiting step. The aggregation reaction model predicts the process will run downhill after this initial conformational change. (v) The reaction model is used to predict the trajectories of oligomers (Supporting Information Fig. S3). The dominant early-predicted species were dimers, and the dimers for A2V exist for hours longer than either A2T or WT (Supporting Information Fig. S3). Shankar *et al.* suggest these dimers are the dominant synaptotoxic species.[26]

Thus, nonmixing *in vitro* aggregation demonstrated that the overall aggregation rate, and specifically k_{mon}, for A2V is much slower than that of A2T and WT, indicating is the most stable monomeric species. Also our model predicts the monomer conformational change is the aggregation's rate limiting step, a feature predicted using independent calculations on a completely different set of $A\beta_{1-42}$ aggregation data.[29]

Consistently, Messa *et al.* have recently reported distinctive aggregation of A2V compared with WT.[8] However, comparing their homozygous aggregation kinetics with our A2V and WT kinetics results, we see that A2V kinetics were much slower than WT with non-mixing and they observe the reverse. This could be explained by the different protocols used by each group, that is we used 12.5 μM at 37°C in PBS and they used 100 μM at 4 or 22°C in phosphate buffer. These differences could have an enormous effect on aggregation rates.[36] See Discussion for further elaboration on this topic.

Comparison of aggregate morphology

The differences in aggregate morphology after aggregation for 18 and 72 h for the mixed and non-mixed runs, respectively, are shown in Figure 2. The following is observed:

With mixing. $A\beta_{1-42}$ aggregation generated fibrils for all three variants with mixing at 1020 rpm [Fig. 2(A)]. The height distribution for A2T and A2V fibrils were similar, that is, 2.1 ± 1.3 nm and 2.6 ± 1.5 nm, respectively. WT aggregated into fibrils under mixing conditions, but with a different distribution compared with A2T and A2V. The WT fibrils were uniformly distributed from 0 to 6 nm and had a mean height of 4.5 ± 2.5 nm. It is possible that the unique height distribution of WT fibrils comes from inherent variability in synthetic peptide production.

Without mixing. For non-mixing aggregation, two unique morphologies existed on each molecularly smooth mica substrate for each variant [Fig. 2(B,C)]. All three variants aggregated into fibrils and an alternate morphology.

(a) Fibrils [Fig. 2(B)]: A2T and A2V fibrils have similar height distribution profiles, that is, 2.8 ± 1.7 nm and 3.1 ± 1.7 nm. The height distribution for WT fibrils shifted from a lognormal-like distribution to a more Gaussian-like distribution, and the mean and standard deviation height of 3.4 ± 1.6 nm was similar for A2T and A2V.

(b) Other aggregates [Fig. 2(C)]: Both WT and A2V formed spherical-like aggregates as an alternative morphology to fibrils, whereas A2T formed proto-fibrils without any evidence of small spherical aggregates. Despite contrasting morphologies of the A2T and WT aggregates, the height distributions of the two species were comparable to the mean and standard deviation of 0.78 ± 0.82 nm (proto-fibrils) and 1.2 ± 0.50 nm (spherical-like aggregates) for A2T and

WT respectively. The spherical aggregates of A2V yielded a height distribution akin to fibrillar species with a mean and standard deviation of 2.3 ± 1.6 nm. This result is in agreement with earlier AFM Aβ morphology images of WT aggregates with non-mixing that showed WT formed fibrils and spherical aggregates.[38]

Here, we have shown that A2T and A2V exhibit different *in vitro* aggregation kinetics, different morphological structures after aggregation (spherical-like vs. proto-fibril structures), and different abundances of smaller oligomers, with "peculiar behavior of A2V oligomers."[8] Distinctive formation of dimers and spherical-like aggregates could both be associated with different mechanisms of decreased/increased pathological effects for A2T/A2V variants of $A\beta_{1-42}$ (see Broerson *et al.*[39] and references therein).

Variant effect on LTP inhibition

Neuronal long term potentiation (LTP), an electrophysiological measurement that correlates with memory and learning, is shown to be inhibited experimentally by soluble Aβ species.[14,26,40,41] To examine the effects of the $A\beta_{1-42}$ variants on neuronal LTP, micromolar concentrations of peptide were dissolved in ACSF (vehicle), applied to mouse hippocampal slices and standard field excitatory postsynaptic potential (fEPSPs) were recorded. The different Aβ variants were treated for at least 30 min before the high frequency stimulation (HFS) being applied. Compared with the vehicle, WT and A2V reduced the slope of the fEPSPs from 150% ± 6.3% (vehicle, $n = 6$) to 123% ± 5.5% (WT, $n = 6$) and 126% ± 5.5% (A2V, $n = 6$), significantly less than the vehicle (P values < 0.001 for WT vs. vehicle, Fig. 3). This result for WT is consistent with previously reported Aβ-induced neuronal LTP inhibition.[23] Interestingly, A2T only slightly decreased the fEPSPs slope to a final value of 140% ± 4.0% ($n = 6$, $P < 0.05$ compared with vehicle), however its LTP inhibition is significantly less than A2V (P values < 0.05). This indicates A2T has less of an effect than WT and A2V on LTP inhibition, a measurement that has previously been correlated with learning and memory loss, and thus provides the first pathologically-relevant evidence toward A2T's reduced causation of AD.

Monomeric structure from experiments

Detailed structural knowledge of the monomeric form of the $A\beta_{1-42}$ variants, that are the minimal building blocks of a complex aggregation process, served to elucidate the differences in their biophysical properties.[42] The structural characterization of the full length $A\beta_{1-42}$ monomeric peptides in solution is extremely challenging through standard ensemble averaging techniques due to their highly disordered nature and a tendency to populate a heterogeneous ensemble of multiple conformations. This is a common feature of amyloidogenic proteins.[43,44] Below, we provide an analysis of the monomer structure for the three variants using CD and IMS-MS experiments.

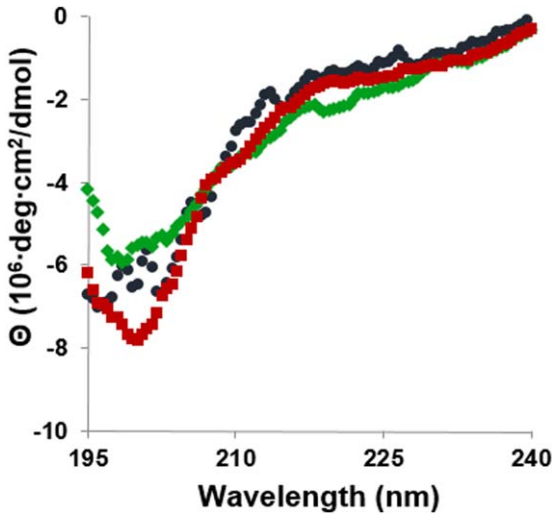

Figure 4

Experimental secondary structure: CD spectra of 25 μ*M* $A\beta_{1-42}$ WT (blue circles), A2T (green diamonds), and A2V (red squares). Unsmoothed data shown in Supporting Information Figure S4. [Color figure can be viewed in the online issue, which is available at wileyonlinelibrary.com.]

Circular dichroism

All three variant monomeric structures according to their CD spectra are dominated by random coil (198 nm) and contain only minor percentages of β-strand (215 nm) and α-helix (222 nm) (smoothed data in Fig. 4 with raw data in Supporting Information Fig. S4). Similar CD spectra for WT and A2V were published by Messa *et al.*[8]

Ion mobility spectrometry-mass spectrometry

The conformation of the different variants was also explored by IMS-MS experiments that are capable of differentiating isomeric species as a function of their ability to interact with buffer gas while traveling through a moderate electric field.[45,46] The ion's conformation determines the rate of interaction, which governs the time necessary to exit the mobility cell. This constitutes the observed experimental mobility. The above approach has been successfully employed to investigate the conformation of different short versions of the $A\beta_{1-42}$ peptide, which provided new insights into the putative mechanism of aggregation.[47,48] We applied this technique to examine the conformations adopted by full-length $A\beta_{1-42}$ and its variants. Figure 5 provides representative time distribution profiles detected in negative ion mode (pI of $A\beta_{1-42}$ is ~5) from the 3-charge state of monomeric WT, A2T and A2V peptides. Displayed under each trace are the results of a curve fitting procedure that was carried out to discriminate the contributions of individual

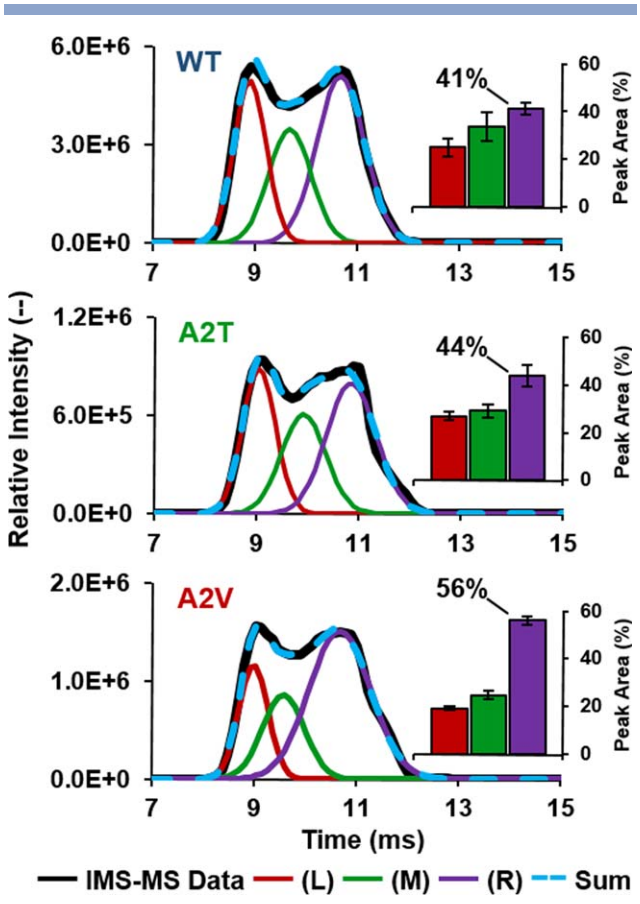

Figure 5

Experimental conformers: IMS-MS profiles and Gaussian-fit curves obtained from monomeric $A\beta_{1-42}$ WT (top), A2T (center), and A2V (bottom). 3-Gausian peaks fitted the raw data mobilograms for all three variants (blue dashed). Matching was based on the arrival time corresponding to the apex of each fitted peak. Peak areas for (L) (red), (M) (green), and (R) (purple) are calculated using numerical error minimization as a percentage of the total peak area and displayed in the inset to the right of each mobiligram. The error bars represent one standard deviation from the average of three fits using distinct initial parameters. The relative standard deviation of the IMS-MS data itself is ±0.01%. The displayed percentage is the peak area percent for (R).

conformers. For each of the variants, the procedure returned three distinctive Gaussian peaks, which were labeled left (L), middle (M), and right (R).

The exact relationship between gas-phase and solution structures is still the object of intense debate in the mass spectrometry community.[49–51] However, the self-consistency of IMS-MS determinations enables one to compare results obtained from different samples and draw general conclusions about their different behaviors and topologies. In our case, the following observations can be made on the basis of the order of arrival times afforded by the detected species, which is determined by their respective conformations. The fact that species (R) displayed longer arrival times than those of (M) and (L) indicates that (R) possesses a more extended conformation (Fig. 5). It has been shown that, in the case of Aβ peptides, extended conformations represent solution-like structures, whereas more compact conformations reflect progressively more dehydrated structures that may be produced during gas-phase analysis.[52] For this reason, the partitioning between the solution-like (R) and the dehydrated (M) and (L) conformers may provide valuable insights into the intrinsic flexibility of the different variants. Based on the area under each peak, which provides a measure of the abundance of the corresponding conformation, the abundance of conformer (R) displays a A2V > WT ~ A2T trend. This observation suggests that the A2V is likely to possess the most stable structure in the series, which is the least prone to the dehydration effects associated with gas-phase analysis. Conversely, the flexibility possessed by A2T makes this variant more sensitive to the transition to a solvent-free environment. Earlier modeling work has suggested that the compact, solvent-free structure has polar residues buried and hydrophobic residues exposed.[42] Additionally previous molecular dynamics simulations show differences in the conformational landscape for these three variants, which is in good agreement with the experimental data presented here.[35]

In summary, we show using low resolution CD that three variants are mainly random coil in nature. With high resolution IMS-MS, we demonstrate that the three variants exhibit very similar, but subtly different, profiles in terms of species populations, which is in good agreement with previously published simulations.[35]

Aβ binding

ApoE receptor-mediated internalization of Aβ by astrocytes and microglia represents a functional pathway to clear and eventually degrade Aβ.[53] Thus, binding of $A\beta_{1-42}$ variants to ApoE isoforms provide guidance to $A\beta_{1-42}$ clearance [Fig. 6(A)]. A2V exhibited the weakest binding to ApoE3 and E4 suggesting that it may clear less efficiently than WT and A2T. Also, note that binding to ApoE4, a positive risk factor for AD,[53,54] was always less than that for ApoE3 perhaps impeding clearance. Also no signal was observed for the scrambled control. EphB2 mediates neuronal NMDA receptor function through binding with $A\beta_{1-42}$.[21] Differences in variant binding to the EphB2-FC chimera, a receptor domain, that is, known to bind $A\beta_{1-42}$,[21] is clear [Fig. 6(B)]. Again, as with the ApoE isoforms, A2V variant binds less to EphB2 than does A2T and WT. Interestingly, comparing the $A\beta_{1-42}$ binding to the EphB2-FC chimera and to itself for A2T and for WT are significantly different (P values < 0.01 for both comparisons), while that for A2V is not significantly different. It appears that A2V binds to this receptor domain and to itself with similar low affinity. It should be noted that dot blot analysis is less accurate in determining binding affinity of specific conformations to target proteins than other (e.g., Surface plasmon resonance) direct measurements.

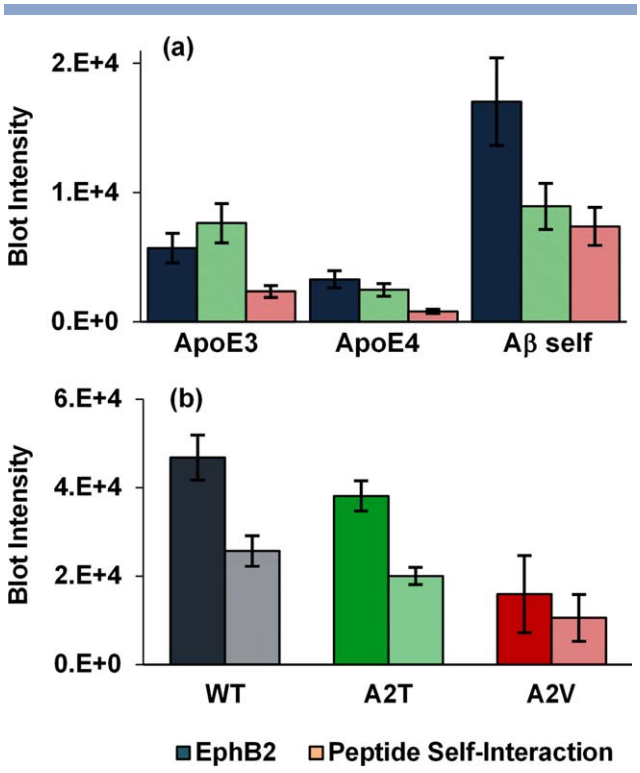

Figure 6

Molecule binding estimation: (**a**) Binding of 12.5 μM Aβ1–42 WT (blue), A2T (green) or A2V (red) to ApoE3, ApoE4 and to themselves (self-binding), as well as (**b**) binding to EphB2 binding domain and themselves (self-binding) as quantified by dot blots. [Color figure can be viewed in the online issue, which is available at wileyonlinelibrary.com.]

DISCUSSION

As mentioned above, a ~20% reduction of $A\beta_{1-42}$ concentration with the A2T variant is attributed to less effective β-secretase cleavage of APP. To offer an alternate explanation to this upstream hypothesis and one related to downstream processing of $A\beta_{1-42}$, the variants should exhibit markedly different aggregation, clearance, binding and LTP inhibition, as reported in this study. We further provide a rational explanation for such different biophysical behavior and how these differences could, in principle, increase necrosis.

The results presented here demonstrate for the first time, to our knowledge, that the protective (A2T) and causative (A2V) variants convert kinetically to proto-fibrils and large spherical aggregates, respectively (Figs. 1 and 2), and exhibit molecular structural and mobility differences (IMS-MS, Fig. 4). In addition, the variants induce distinct LTP inhibition, a pathologically relevant result not previously reported (Fig. 3). Further, the variants offer diverse binding to ApoE isoforms and receptor domains. These downstream events during the Aβ cascade, from dual cleavage of APP to oligomer aggregation, fibril formation, and clearance, are integral to maintaining a dynamic steady state flow of Aβ into and out of the cell. Any change in the biophysical properties such as those observed for A2V, for example, slower aggregation kinetics and hence longer residence time for oligomers, with structural dimers and trimers at lower frequency than those of A2T and WT, poorer binding to ApoE isoforms suggesting lower clearance, would result in its buildup. Converse behavior regarding structural oligomers partly different from those of WT and A2V as well as ApoE and receptor binding, was observed for the A2T variant, suggesting early proto-fibril formation with recruitment of toxic oligomers via a less toxic pathway compared with the WT and A2V. If, as the Selkoe group has reported,[26] dimers are the smallest synaptotoxic oligomers, then our reaction model predicts for non-mixing that the dimers endure markedly longer for A2V than for WT/A2T (Supporting Information Fig. S3, right two top plots).

A comparison of aggregate morphology and especially the heights for the three variants suggest that fibrils generated with and without mixing were similar for all three variants within error of the measurements. However, the main morphological difference was between other aggregates. WT and A2V formed small and larger spherical-like aggregates, respectively, while A2T only formed small height proto-fibrils without any spherical-like structures. This finding could be significant, given that the spherical-like "doughnut" aggregates intercalate into cell membranes and induce slow ionic leakage through central pores.[55] Thus, one could speculate that the mechanism of protection against "toxicity" or slow cell leakage for A2T relies on its ability to recruit spherical-like "doughnut" aggregates out of the solution and into proto-fibrils, thus protecting the cells from ion leakage, whereas A2V's toxic mechanism is derived from its ability to remain in the dimeric/small oligomeric state for substantially longer than both WT and A2T (Supporting Information Fig. S2). Clearly, more work needs to be done on fractionating these structures and testing their separate toxicity with neuronal cells or in mice that overexpress Aβ.[56–58]

As mentioned above, $A\beta_{1-42}$ aggregation kinetics from two recent publications report dissimilar results from the ones presented here, which is that A2V has a drastically longer lag time (16 ± 1.0 h) than A2T (3.6 ± 0.19 h) which in turn has a slightly longer lag time than WT (2.3 ± 0.13 h) (Fig. 1).[16,17] The experiments here are designed to capture the rate of primary nucleation of the Aβ variants whereas both Maloney *et al.* and Benilova *et al.* report little or no lag time in their aggregation experiments, indicating bypass of primary nucleation, likely due to experimental seeding (see Supporting Information Table SIII).[16,17] Therefore, they fail to capture the substantial differences reported here in terms of primary nucleation (Fig. 1).

As predicted by our model and supported by the IMS-MS data (Fig. 5) and previous MD simulations,[35]

the main difference in aggregation behavior without mixing emanates from the initial monomer structural stability.[29]

Here, clear differences in the lag time for the aggregation of WT (2.3 ± 0.13 h), A2T (3.6 ± 0.19 h) and A2V (16 ± 1.0 h), due mainly to substantially slower rate of monomer unfolding for A2V (Fig. 1). Thus, the IMS-MS data, the aggregation results and modeling show the A2V monomer is the most stable, at least in terms of species dehydration, whereas the WT and A2T monomers are considerably less so (Fig. 5), a result, that is, supported by recent MD simulations.[35] These results bolster the overall picture that the stability of the variant monomers is markedly different, and this effect, while not observed in aggregation experiments dominated by secondary nucleation,[16,17] is clearly demonstrated and modeled for aggregation kinetics that incorporate primary nucleation.

In addition, the CD results (Fig. 4) are in good agreement with published CD results[8] confirming that our monomer secondary structures are similar and not aberrant.

Presented here for the first time is a biophysically relevant property of A2T, that is, LTP inhibition, that relates directly with the protection of AD.[14,26,40,41] The LTP inhibition of hippocampal cells, which correlates with memory formation, is markedly less for A2T (140% ± 4.0%) than both WT (123% ± 5.5%) and A2V (126% ± 5.5%, Fig. 3). As has been reported, A2T reduces the β-secretase cleavage rate of APP resulting in a ~20% reduction in $A\beta_{1-42}$ monomer concentration, while A2V effects cleavage conversely.[8,17] Here, we show that A2T reduces LTP inhibition in comparison with WT, a result that demonstrates a pathway toward reduced causation of AD for this protective mutant. Hence, we speculate that conformational differences between A2T and A2V are the cause of the differences in LTP inhibition and provide additional evidence for reduced and enhanced causation of AD, respectively.

If, as we suspect and have demonstrated here, downstream events are critical for synaptotoxicity, then intervention at each downstream step may be possible. Options include complete inhibition of oligomerization (Fig. 1), preventing formation of large spherical-like structures (Fig. 2), mild stabilization of monomer conformation (Figs. 1 and 5), and/or increasing ApoE binding (Fig. 6). Small molecules have been designed and synthesized to bind with $A\beta_{1-42}$.[59,60] They could possibly be specifically designed for the A2V variant to inhibit aggregation and/or to increase binding to ApoE isoforms. Upregulating the ApoE gene for increased A2V clearance may also help.[9,53] The role of the extreme N-terminus in modulating $A\beta_{1-42}$ monomer structure, aggregation, LTP inhibition, and clearance obtained here can also guide design of inhibitory peptides against the N-terminus (i.e., aducanumab).

ACKNOWLEDGMENTS

The authors thank Marlene Belfort, Biology Department, University at Albany, for laboratory assistance, C. Seth Pearson and Hon Chan from the group for dot blot assay, Jianjun Wang, Wayne State University School of Medicine, for recombinant ApoE isomers, Dennis Selkoe, Brigham and Women's hosptial and Harvard Medical School, for suggesting the LTP experiments, and Marlene Belfort and Gabriel Belfort, Sage Therapeutics, for comments on the manuscript.

REFERENCES

1. Shankar GM, Bloodgood BL, Townsend M, Walsh DM, Selkoe DJ, Sabatini BL. Natural oligomers of the Alzheimer amyloid-beta protein induce reversible synapse loss by modulating an NMDA-type glutamate receptor-dependent signaling pathway. J Neurosci Off JSoc Neurosci 2007;27:2866–2875.
2. Fandrich M. Oligomeric intermediates in amyloid formation: structure determination and mechanisms of toxicity. J Mol Biol 2012; 421:427–440.
3. Hardy J, Selkoe DJ. The amyloid hypothesis of Alzheimer's disease: progress and problems on the road to therapeutics. Science 2002; 297:353–356.
4. Goate A, Hardy J. Twenty years of Alzheimer's disease-causing mutations. J Neurochem 2012;120:3–8.
5. Jonsson T, Atwal JK, Steinberg S, Snaedal J, Jonsson PV, Bjornsson S, Stefansson H, Sulem P, Gudbjartsson D, Maloney J, Hoyte K, Gustafson A, Liu Y, Lu Y, Bhangale T, Graham RR, Huttenlocher J, Bjornsdottir G, Andreassen OA, Jonsson EG, Palotie A, Behrens TW, Magnusson OT, Kong A, Thorsteinsdottir U, Watts RJ, Stefansson K. A mutation in APP protects against Alzheimer's disease and age-related cognitive decline. Nature 2012;488:96–99.
6. Peacock ML, Warren JT, Roses AD, Fink JK. Novel polymorphism in the A4 region of the amyloid precursor protein gene in a patient without Alzheimer's disease. Neurology 1993;43:1254–1254.
7. Di Fede G, Catania M, Morbin M, Rossi G, Suardi S, Mazzoleni G, Merlin M, Giovagnoli AR, Prioni S, Erbetta A, Falcone C, Gobbi M, Colombo L, Bastone A, Beeg M, Manzoni C, Francescucci B, Spagnoli A, Cantu L, Del Favero E, Levy E, Salmona M, Tagliavini F. A recessive mutation in the APP gene with dominant-negative effect on amyloidogenesis. Science 2009;323:1473–1477.
8. Messa M, Columbo L, del Favero E, Cantu L, Stoilova T, Cagnotto A, Rossi A, Morbin M, Di Fede G, Tagliavini F, Salmona M. The perculiar role of the A2V mutation in amyloid-beta (Abeta) 1-42 molecular assembly. J Biol Chem 2014;289:24143–24152.
9. Cramer PE, Cirrito JR, Wesson DW, Lee CY, Karlo JC, Zinn AE, Casali BT, Restivo JL, Goebel WD, James MJ, Brunden KR, Wilson DA, Landreth GE. ApoE-directed therapeutics rapidly clear beta-amyloid and reverse deficits in AD mouse models. Science 2012; 335:1503–1506.
10. Benilova I, De Strooper B. Neuroscience. Promiscuous Alzheimer's amyloid: yet another partner. Science 2013;341:1354–1355.
11. Kim T, Vidal GS, Djurisic M, William CM, Birnbaum ME, Garcia KC, Hyman BT, Shatz CJ. Human LilrB2 is a beta-amyloid receptor and its murine homolog PirB regulates synaptic plasticity in an Alzheimer's model. Science 2013;341:1399–1404.
12. Kam TI, Song S, Gwon Y, Park H, Yan JJ, Im I, Choi JW, Choi TY, Kim J, Song DK, Takai T, Kim YC, Kim KS, Choi SY, Choi S, Klein WL, Yuan J, Jung YK. FcgammaRIIb mediates amyloid-beta neurotoxicity and memory impairment in Alzheimer's disease. J Clin Investig 2013;123:2791–2802.
13. Verdier Y, Zarandi M, Penke B. Amyloid beta-peptide interactions with neuronal and glial cell plasma membrane: binding sites and implications for Alzheimer's disease. J Peptide Sci Off Publ Eur Peptide Soc 2004;10:229–248.
14. Selkoe DJ. Alzheimer's disease is a synaptic failure. Science 2002; 298:789–791.

15. Dimitrov M, Alattia JR, Lemmin T, Lehal R, Fligier A, Houacine J, Hussain I, Radtke F, Dal Peraro M, Beher D, Fraering PC. Alzheimer's disease mutations in APP but not gamma-secretase modulators affect epsilon-cleavage-dependent AICD production. Nat Commun 2013;4:2246.
16. Benilova I, Gallardo R, Ungureanu AA, Castillo Cano V, Snellinx A, Ramakers M, Bartic C, Rousseau F, Schymkowitz J, De Strooper B. The Alzheimer disease protective mutation A2T modulates kinetic and thermodynamic properties of amyloid-beta (Abeta) aggregation. J Biol Chem 2014;289:30977–30989.
17. Maloney JA, Bainbridge T, Gustafson A, Zhang S, Kyauk R, Steiner P, van der Brug M, Liu Y, Ernst JA, Watts RJ, Atwal JK. Molecular mechanisms of Alzheimer disease protection by the A673T allele of amyloid precursor protein. J Biol Chem 2014;289:30990–31000.
18. De Strooper B, Voet T. Alzheimer's disease: a protective mutation. Nature 2012;488:38–39.
19. Wolf LK. Alzheimer's treatment dispute. Chem Eng News 2013;91:2.
20. Fitz NF, Cronican AA, Lefterov I, Koldamova R. Comment on "ApoE-directed therapeutics rapidly clear beta-amyloid and reverse deficits in AD mouse models." Science 2013;340:924–c.
21. Cisse M, Halabisky B, Harris J, Devidze N, Dubal DB, Sun B, Orr A, Lotz G, Kim DH, Hamto P, Ho K, Yu GQ, Mucke L. Reversing EphB2 depletion rescues cognitive functions in Alzheimer model. Nature 2011;469:47–52.
22. Ban T, Hamada D, Hasegawa K, Naiki H, Goto Y. Direct observation of amyloid fibril growth monitored by thioflavin T fluorescence. J Biol Chem 2003;278:16462–16465.
23. Li S, Jin M, Koeglsperger T, Shepardson NE, Shankar GM, Selkoe DJ. Soluble Aβ oligomers inhibit long-term potentiation through a mechanism involving excessive activation of extrasynaptic NR2B-containing NMDA receptors. J Neurosci 2011;31:6627–6638.
24. Li S, Hong S, Shepardson NE, Walsh DM, Shankar GM, Selkoe D. Soluble oligomers of amyloid β protein facilitate hippocampal long-term depression by disrupting neuronal glutamate uptake. Neuron 2009;62:788–801.
25. Li S, Jin M, Zhang D, Yang T, Koeglsperger T, Fu H, Selkoe DJ. Environmental novelty activates β 2-adrenergic signaling to prevent the impairment of hippocampal LTP by Aβ oligomers. Neuron 2013;77:929–941.
26. Shankar GM, Li S, Mehta TH, Garcia-Munoz A, Shepardson NE, Smith I, Brett FM, Farrell MA, Rowan MJ, Lemere CA, Regan CM, Walsh DM, Sabatini BL, Selkoe DJ. Amyloid-beta protein dimers isolated directly from Alzheimer's brains impair synaptic plasticity and memory. Nat Med 2008;14:837–842.
27. Wiberg HEP, Pettersson FE, Lannfelt L, Emmer A, Roeraade J. Separation and characterization of aggregated species of amyloid-beta peptides. Anal Bioanal Chem 2010;397:10.
28. Knowles TP, Waudby CA, Devlin GL, Cohen SI, Aguzzi A, Vendruscolo M, Terentjev EM, Welland ME, Dobson CM. An analytical solution to the kinetics of breakable filament assembly. Science 2009;326:1533–1537.
29. Ferrone FA. Assembly of Abeta proceeds via monomeric nuclei. J Mol Biol 2015;427:287–290.
30. Lee CC, Nayak A, Sethuraman A, Belfort G, McRae GJ. A three-stage kinetic model of amyloid fibrillation. Biophys J 2007;92:3448–3458.
31. Serio TR, Cashikar AG, Kowal AS, Sawicki GJ, Moslehi JJ, Serpell L, Arnsdorf MF, Lindquist SL. Nucleated conformational conversion and the replication of conformational information by a prion determinant. Science 2000;289:1317–1321.
32. Heldt CL, Zhang SQ, Belfort G. Asymmetric amyloid fibril elongation: a new perspective on a symmetric world. Proteins Struct Funct Bioinform 2011;79:92–98.
33. Liu C-C, Kanekiyo T, Xu H, Bu G. Apolipoprotein E and Alzheimer disease: risk, mechanisms and therapy. Nat Rev Neurol 2013;9:106–118.
34. Cohen SI, Linse S, Luheshi LM, Hellstrand E, White DA, Rajah L, Otzen DE, Vendruscolo M, Dobson CM, Knowles TP. Proliferation of amyloid-beta42 aggregates occurs through a secondary nucleation mechanism. Proc Natl Acad Sci USA 2013;110:9758–9763.
35. Das P, Murray B, Belfort G. Alzheimer's protective A2T mutation changes the conformational landscape of the Aβ 1–42 monomer differently than does the A2V mutation. Biophys J 2015;108:738–747.
36. Nielsen L, Khurana R, Coats A, Frokjaer S, Brange J, Vyas S, Uversky VN, Fink AL. Effect of environmental factors on the kinetics of insulin fibril formation: elucidation of the molecular mechanism. Biochemistry 2001;40:6036–6046.
37. Sorci M, Grassucci RA, Hahn I, Frank J, Belfort G. Time-dependent insulin oligomer reaction pathway prior to fibril formation: cooling and seeding. Proteins 2009;77:62–73.
38. Ladiwala AR, Litt J, Kane RS, Aucoin DS, Smith SO, Ranjan S, Davis J, Van Nostrand WE, Tessier PM. Conformational differences between two amyloid beta oligomers of similar size and dissimilar toxicity. JBiol Chem 2012;287:24765–24773.
39. Broersen K, Rousseau F, Schymkowitz J. The culprit behind amyloid beta peptide related neurotoxicity in Alzheimer's disease: oligomer size or conformation? Alzheimer's Res Ther 2010;2:12.
40. Walsh DM, Klyubin I, Fadeeva JV, Cullen WK, Anwyl R, Wolfe MS, Rowan MJ, Selkoe DJ. Naturally secreted oligomers of amyloid β protein potently inhibit hippocampal long-term potentiation in vivo. Nature 2002;416:535–539.
41. Wilcox KC, Lacor PN, Pitt J, Klein WL. Aβ oligomer-induced synapse degeneration in Alzheimer's disease. Cell Mol Neurobiol 2011;31:939–948.
42. Bernstein SL, Wyttenbach T, Baumketner A, Shea JE, Bitan G, Teplow DB, Bowers MT. Amyloid beta-protein: monomer structure and early aggregation states of Abeta42 and its Pro19 alloform. J Am Chem Soc 2005;127:2075–2084.
43. Mukhopadhyay S, Krishnan R, Lemke EA, Lindquist S, Deniz AA. A natively unfolded yeast prion monomer adopts an ensemble of collapsed and rapidly fluctuating structures. Proc Natl Acad Sci USA 2007;104:2649–2654.
44. Uversky VN, Eliezer D. Biophysics of Parkinson's disease: structure and aggregation of alpha-synuclein. Curr Protein Peptide Sci 2009;10:483–499.
45. Clemmer DE, Jarrold AG. Ion mobility measurements and their application to cluster biomolecules. J Mass Spectrometry 1997;32:15.
46. Kanu AB, Dwivedi P, Tam M, Matz L, Hill HH, Jr. Ion mobility-mass spectrometry. J Mass Spectrom 2008;43:1–22.
47. Bleiholder C, Do TD, Wu C, Economou NJ, Bernstein SS, Buratto SK, Shea JE, Bowers MT. Ion mobility spectrometry reveals the mechanism of amyloid formation of Abeta(25-35) and its modulation by inhibitors at the molecular level: epigallocatechin gallate and scyllo-inositol. J Am Chem Soc 2013;135:16926–16937.
48. Bleiholder C, Dupuis NF, Wyttenbach T, Bowers MT. Ion mobility-mass spectrometry reveals a conformational conversion from random assembly to beta-sheet in amyloid fibril formation. Nat Chem 2011;3:172–177.
49. Ruotolo BT, Robinson CV. Aspects of native proteins are retained in vacuum. Curr Opin Chem Biol 2006;10:402–408.
50. Breuker K, McLafferty FW. Stepwise evolution of protein native structure with electrospray into the gas phase, 10− 12 to 102 s. Proc Natl Acad Sci 2008;105:18145–18152.
51. Balthasart F, Plavec J, Gabelica V. Ammonium ion binding to DNA G-quadruplexes: do electrospray mass spectra faithfully reflect the solution-phase species? J Am Soc Mass Spectrom 2013;24:1–8.
52. Baumketner A, Bernstein SL, Wyttenbach T, Bitan G, Teplow DB, Bowers MT, Shea JE. Amyloid beta-protein monomer structure: a computational and experimental study. Protein Sci Publ Protein Soc 2006;15:420–428.

53. Bu G. Apolipoprotein E and its receptors in Alzheimer's disease: pathways, pathogenesis and therapy. Nat Rev Neurosci 2009;10:333–344.
54. Chen J, Li Q, Wang J. Topology of human apolipoprotein E3 uniquely regulates its diverse biological functions. Proc Natl Acad Sci USA 2011;108:14813–14818.
55. Quist A, Doudevski I, Lin H, Azimova R, Ng D, Frangione B, Kagan B, Ghiso J, Lal R. Amyloid ion channels: a common structural link for protein-misfolding disease. Proc Natl Acad Sci USAm 2005;102:10427–10432.
56. Stohr J, Condello C, Watts JC, Bloch L, Oehler A, Nick M, DeArmond SJ, Giles K, DeGrado WF, Prusiner SB. Distinct synthetic Abeta prion strains producing different amyloid deposits in bigenic mice. Proc Natl Acad Sci USA 2014;111:10329–10334.
57. Watts JC, Condello C, Stohr J, Oehler A, Lee J, DeArmond SJ, Lannfelt L, Ingelsson M, Giles K, Prusiner SB. Serial propagation of distinct strains of Abeta prions from Alzheimer's disease patients. Proc Natl Acad Sci USA 2014;111:10323–10328.
58. Abatemarco T, Stickel J, Belfort J, Frank BP, Ajayan PM, Belfort G. Fractionation of multi-walled carbon nanotubes by cascade membrane microfiltration. J Phys Chem B 1999;103:5.
59. Rzepecki P, Wehner M, Molt O, Zadmard R, Harms K, Schrader T. Aminopyrazole oligomers for beta-sheet stabilization of peptides. Synthesis Stuttgart 2003;12:1815–1826.
60. Rzepecki P, Schrader T. beta-Sheet ligands in action: KLVFF recognition by aminopyrazole hybrid receptors in water. J Am Chem Soc 2005;127:3016–3025.